atmosphere

MDPI

Article

Paleoclimate Controls on West African Dust Inferred from Rb/Sr and Si/Al of Sediments in an Eastern Equatorial Atlantic Marine Core

Christopher J. Lepre [1,*], Clara Y. Chang [2] and Owen M. Yazzie [1]

[1] School of Earth, Environment and Society, Bowling Green State University, Bowling Green, OH 43403, USA; oyazzie@bgsu.edu
[2] Lamont-Doherty Earth Observatory, Columbia University, New York, NY 10964, USA; cchang@ldeo.columbia.edu
* Correspondence: leprecj@bgsu.edu; Tel.: +1-419-372-7632

Abstract: Increased dust emissions from dryland areas and their effects on human health, ecosystem viability, and environmental change are a global concern in the face of the growing climate crisis. Dust plume emissions from the West African landmass, Sahara, and Sahel areas comprise a major fraction of the global aerosol budget. Dust plume intensity is closely related to regional winds (e.g., Harmattan, Sahara Air Layer), the Intertropical Convergence Zone, monsoonal seasonality, marine currents, and physiography. To study terrigenous material emitted from the continent over the last ~260 kyr (late Quaternary), we used X-ray fluorescence spectroscopy (XRF) to analyze a ~755 cm long marine sediment core from the eastern equatorial Atlantic Ocean, resulting in nearly 1400 discrete measurements. Spectral analysis results suggest that concentrations of elements (Rb, Sr, Si, Al) preserved in the sediments are correlated to different types of orbital climate forcing. Chemical weathering intensity indicated by the Rb/Sr ratio was sensitive to seasonal insolation variations controlled by precession cycles (23–18 kyr), which presumably reflects the relationship between monsoonal rainfall and sensible heating of the continent. Spectral analysis of silicate mineral grain size (Si/Al) showed significant 40 kyr cycles that were paced by obliquity. Based on these data, we infer that winter tradewind activity accelerated in response to the intertropical insolation gradient induced by high obliquity. High Rb/Sr ratios during the last glacial maximum and penultimate glacial maximum may have been due to a predominance of mechanical weathering over chemical weathering under dry/cool climates or the dissolution of Sr-bearing carbonates by corrosive glacial bottom waters.

Keywords: dust plume; West African monsoon; XRF; terrigenous material; marine sediment core; insolation variations; obliquity; orbital climate cycles; paleoclimate; quaternary

check for updates

Citation: Lepre, C.J.; Chang, C.Y.; Yazzie, O.M. Paleoclimate Controls on West African Dust Inferred from Rb/Sr and Si/Al of Sediments in an Eastern Equatorial Atlantic Marine Core. *Atmosphere* **2024**, *15*, 902. https://doi.org/10.3390/atmos15080902

Academic Editors: Yougui Song and Chaofeng Fu

Received: 30 May 2024
Revised: 16 July 2024
Accepted: 19 July 2024
Published: 28 July 2024

Copyright: © 2024 by the authors. Licensee MDPI, Basel, Switzerland. This article is an open access article distributed under the terms and conditions of the Creative Commons Attribution (CC BY) license (https://creativecommons.org/licenses/by/4.0/).

1. Introduction

Dust is an important environmental component of the atmosphere of Earth and other planets [1,2]. It can affect global climate change by fertilizing terrestrial and marine ecosystems and increasing primary productivity [3,4]. Dust aerosol exposure is an ongoing concern for public health and respiratory illness [5,6]. This is underscored by the recent United Nations' commitment to combating sand and dust storms [7].

One of the main sources of atmospheric dust for Earth is the North African Sahara–Sahel region (Figure 1) and Quaternary sediments of paleo-Lake Chad in the Bodélé Depression [8,9]. North African dust production and transport relate to the seasonality of the West African monsoon [10–12]. During the summer wet season (JJA), the monsoonal front progressively migrates northward and draws in Gulf of Guinea moisture that rains out over the continent [13,14]. This is associated with the summer dust plumes of the Sahara Air Layer/African Easterly Jet [15–17]. The summer plume mostly follows a ~subtropical

latitude over the Atlantic Ocean but also disperses northward into Europe [18,19]. During the winter dry season (DJF), the position of the front and maximum rainfall moves toward the south, leaving the Sahara–Sahel windswept by the Northeast Tradewinds and the Harmattan that carry dust plumes southwestward off the continent [6,20]. Mineral phases in the dust include fine-silt particles of clay, quartz, carbonate, and iron oxides that impart the noticeable red and yellow colors in satellite imagery [19,21–23].

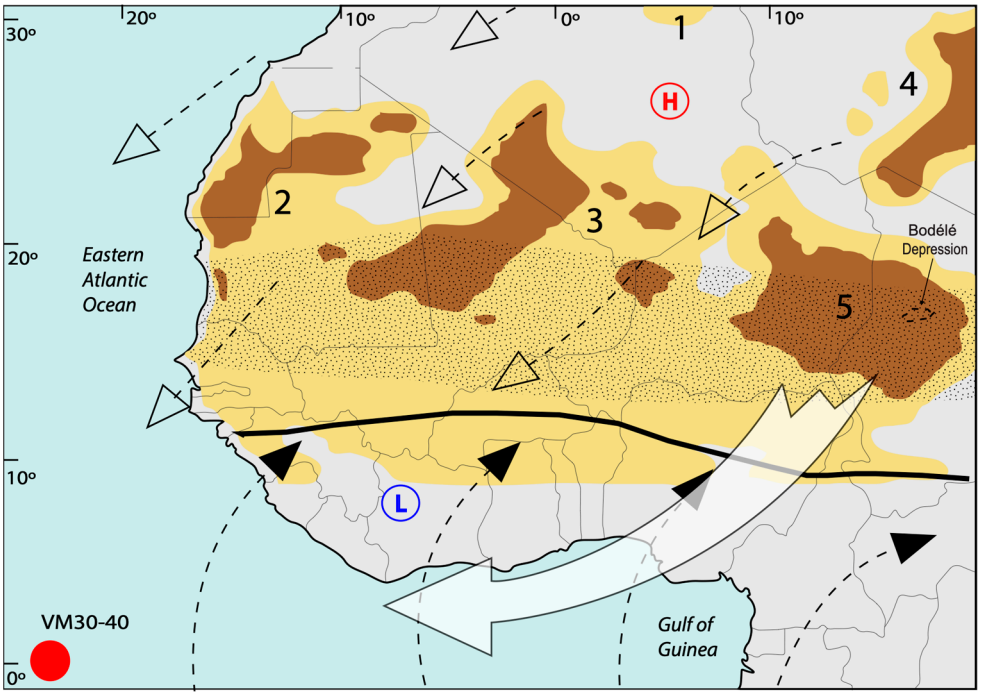

Figure 1. Study location. Climatological features are idealized, and the reader should note that positions of the winds, air masses, and monsoonal flows are changing throughout the year: open arrows are tradewinds; closed arrows monsoonal; high (H) and low (L) pressure; thick, black line is ITCZ; and large arrow is Harmattan. Stippled area is approximate position of the Sahel [16]. Dark brown is areas producing significance dust for 21–31 days; yellow is significant dust production over 7–21 days [24]. Numbers refer to the potential source areas of Scheuvens et al. [23]. For the broader geographic context of VM30–40, the reader is referred to Figure 2.

On geologic timescales, orbital cycles control insolation variations that change the monsoonal intensity and aeolian dust flux from North Africa [25–34]. Orbital precession (~20 kyr) is a fundamental driver of tropical insolation; eccentricity modulates the amplitude and timing of precession [35,36]. Precession shifts the location of the solstices and equinoxes within the orbit, whereas eccentricity determines the Earth–Sun distance. Rainfall increases when precession places monsoonal wet seasons at perihelion [37,38]. However, obliquity (tilt axis) control on tropical insolation budgets also figures prominently in current debates about the role that orbital climate forcing plays in the African monsoon [39,40]. These obliquity debates are concerned with the interhemispheric disparities during the solstices and may have implications for understanding the summer and winter seasonal dust plumes of northern Africa.

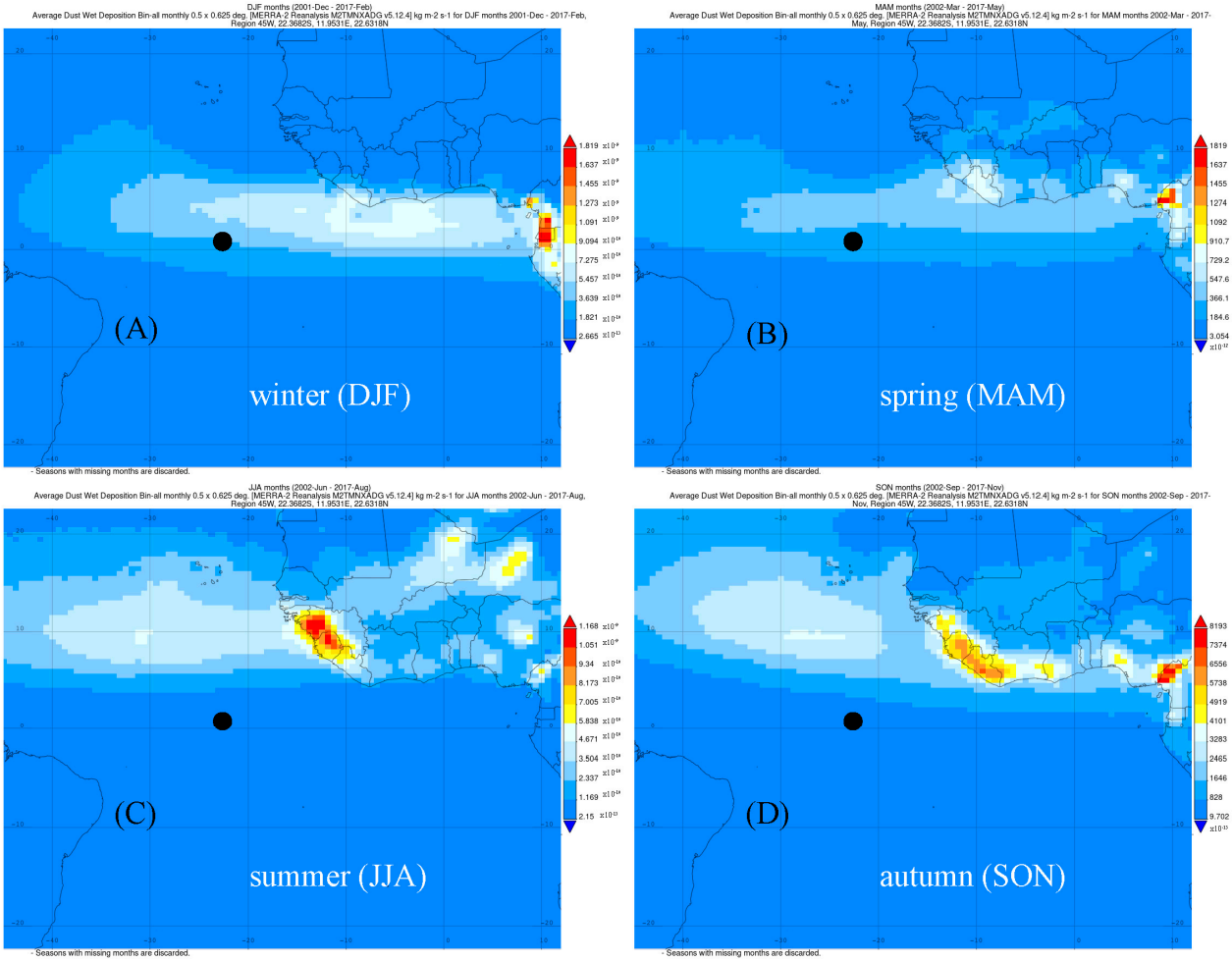

Figure 2. Wet dust deposition during years 2002–2017; winter extends to December of 2001. Wet deposition is the removal of atmospheric gases or aerosols by precipitation. Map-model data accessed through the NASA Giovanni website, from the Modern-Era Retrospective analysis for Research and Applications, Version 2 (MERRA—2). Colors and scale bar at the right of each panel indicate dust deposition units of kg m^{-2} s^{-1}. Panels show deposition during: (**A**) December, January, and February (DJF); (**B**) March, April, May (MAM); (**C**) June, July, August (JJA); and (**D**) September, October, November (SON). Warmer colors symbolize increased rate of deposition. For possible source areas of the dust, the reader is referred to Figure 1. Location of VM30–40 indicated by black circle.

High-latitude climate, polar icesheets, and subsequent effects on low-latitude climates influence the African monsoon and dust variations [29,41–44]. Icesheet expansion in the northern hemisphere creates a stronger north-to-south temperature gradient that may weaken the African monsoon through displacement of the Intertropical Convergence Zone (ITCZ) [45,46]. Icesheet melting in the southern hemisphere leads to changes in ocean water temperature that disrupts the Atlantic Meridional Overturning Circulation [47]. This may cool the North Atlantic by reducing meridional heat transport, which is associated with a southern shift of the ITCZ and a weaker West African monsoon that reduces moisture over tropical North Africa [48,49]. Quaternary glacial–interglacial oscillations are paced by obliquity (~40 kyr) and short eccentricity (~100 kyr). Just prior to the beginning of the Middle Pleistocene (~0.8 Ma), the main period of these oscillations shifted from obliquity to eccentricity [50]. This Mid-Pleistocene climate transition is the subject of much debate, and it appears that obliquity pacing of glacial–interglacial cycles continued into the later part of the Quaternary [51–53]. West African dust-flux records demonstrate a shift occurring near the Mid-Pleistocene transition and earlier during the onset (~2.5–3.0 Ma) of northern

hemisphere glaciations [43,54]. However, there is some debate about the impact of the onset and intensification of the glaciations on Plio-Pleistocene African climate [55,56]. Some studies [26,32] have pointed out that, rather than a direct climate imprint, glacial cycles are known to induce a diagenetic bias on the preservation of West African dust in marine sediment cores. Glacial conditions may result in changes in Atlantic Ocean chemistry that influence carbonate preservation and dissolution in deep water sedimentary environments. This may lead to spurious evidence for glacial controls on monsoonal rainfall and dust in the marine records. Because of these uncertainties, several outstanding questions remain for understanding African paleoclimate: (1) Is dust production sensitive to glacial forcing and its effects on the monsoon rainfall? (2) Considering that marine sediment core evidence has been collected from subtropical sites under the summer dust plume [20,32,48], what do the records indicate from equatorial sites under the winter dust plume?

Presented herein is a restudy of the terrigenous sediments in marine core VEMA core 30–40 (VM30–40). This core was retrieved from the equator (0°12′ S, 20°09′ W) at a water depth of 3706 m. The core spans the last ~260,000 years of the late Quaternary, and the timespan is well constrained with marine oxygen isotope stages [57,58]. Pokras and Mix [59,60] studied VM30–40, suggesting that the freshwater diatom fraction of the sediments derived from monsoonal climate change and aeolian processes associated with the winter West African dust plume (Figure 2). However, the eastern equatorial Atlantic Ocean also sees dust deposition throughout the spring (Figure 2), which suggests that VM30–40 may capture multiple seasons of terrigenous input. Eolian-transported, freshwater diatoms in the marine sediment cores of West Africa derive from the deflation of diatomaceous sediments in dry North African lakebeds [42]. During times of a dry monsoon, lower lake levels exposed diatomite beds that then eroded and became entrained by winds. Thus, the diatom increases in the marine core are thought of as indirect indicators of lake levels and aridity. Spectral analyses conducted for evidence of orbital climate forcing in the VM30–40 freshwater diatom record revealed strong power at precession periods [59]. However, Pokras and Mix [59] noted secondary increases in freshwater diatoms coinciding with marine isotope stages 2, 4, and 6, suggesting that, in addition to climatic precession, glacial epochs and other orbital periods may be recorded by the terrigenous sediments preserved in the core. We explored orbitally paced changes in climate by using X-ray fluorescence spectroscopy (XRF) analysis to reexamine a historic paleoclimate record from sediment core VM30–40 (Figure 3). Our goal was to assess the influences on late Pleistocene terrigenous sediment preservation in the eastern equatorial Atlantic and interpret orbital controls on African paleoclimate through the spectral analysis of the silicon (Si), aluminum (Al), rubidium (Rb), and strontium (Sr) composition of the VM30–40 record. These elements are common to continental detritus and used in African paleoclimate studies to identify the terrigenous fractions of marine cores [30,48,61–63]. The objectives of this research were threefold: (1) develop a stratigraphic timeseries for the XRF measurements using the previously reported sedimentation rate based upon marine isotope stages (MIS); (2) use spectral analysis to resolve orbital periods from the timeseries; and (3) interpret the origins of the orbital periods. This dataset provides additional observations that refine our understanding of monsoonal paleoclimate change and geological controls on past changes in African dust production.

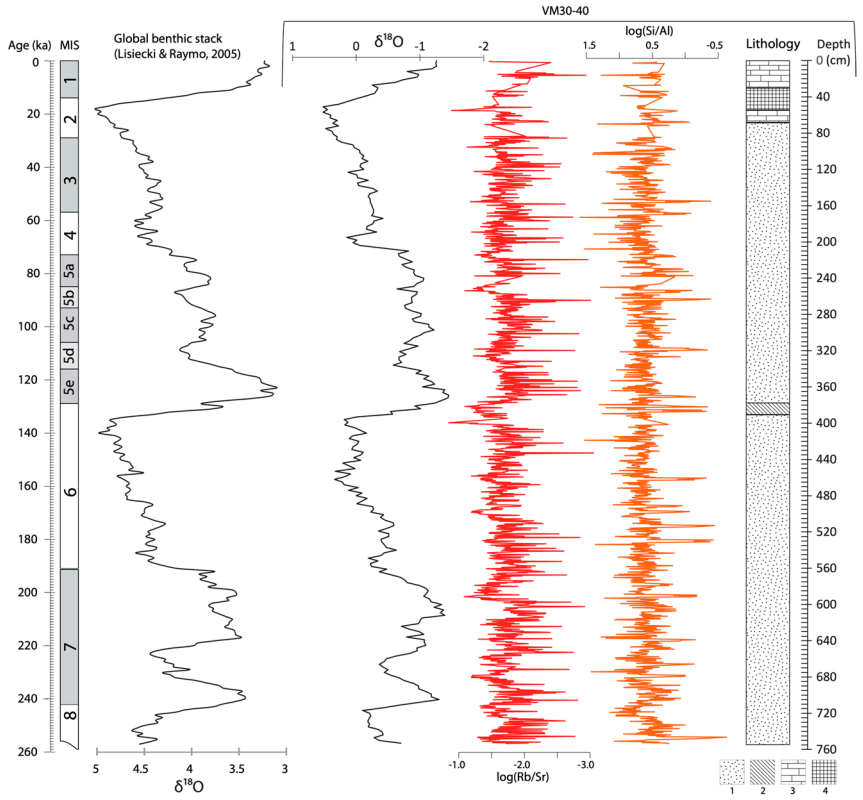

Figure 3. Stratigraphy of VM30—40. Marine isotope stages (MIS) and oxygen isotope curve at left are after Lisiecki and Raymo [50]. Oxygen isotope curve of VM30–40 is from Imbrie et al. and McIntyre et al. [57,58]. All δ18O units are in per mil (0/00). Lithostratigraphy of the core is based on archival information of the Lamont Geological Observatory. Lithological symbols: (1) interbedded layers of foraminiferal ooze and foraminiferal marl ooze, (2) foraminiferal marl, (3) foraminiferal ooze, and (4) foraminiferal marl ooze. The original XRF counts for each record is provided by the Supplementary Material.

2. Materials and Methods

2.1. Marine Core VM30–40

In this paper, we provide new data for VM30–40 (IGSN number DSR000ZD0). This core was initially split and described in 1973 and has been archived at the Lamont-Doherty Core Repository. Prior analysis of VM30–40 indicates that the recovered sediment record has a well-resolved chronostratigraphy (Table 1). The core is 755 cm long, representing the last ~256.7 kyr to late MIS 8 [57,58]. We used the MIS age–depth data (Table 1) to construct a chronology for the core and linearly interpolate a mean sediment accumulation rate of 1 cm per 340 years. VM30–40 has the typical sediments of the marine cores of the eastern tropical Atlantic dominated by biogenic $CaCO_3$ and a subordinate amount of terrigenous detritus [26,30,32,64–66]. Core sediments also contain minor fractions of biogenic opal and phytoliths and may preserve pollen [42,67–69]. Previously, VM30–40 has been used for paleoceanographic and paleoclimate research based on diatoms, phytoliths, $CaCO_3$, color/iron-oxide content, isotopes, and thorium-normalized dust concentrations [57,58,64,65,70,71].

Table 1. VM30–40 core chronology *.

MIS Substage ‡	Age (ka)	Depth (cm)
nr	1.5	0
1.1	6.5	12
2.0	12	33

Table 1. *Cont.*

MIS Substage ‡	Age (ka)	Depth (cm)
2.22	17.8	58.5
2.24	21.4	75
3.0	24	91.5
3.3	53	162
4.0	59	183
4.2	65	195
5.0	71	208
5.1	80	241.5
5.2	87	261
5.3	99	297
5.5	122	370.5
6.0	128	387
6.2	135	399
6.4	151	462
6.5	171	522
nr	176	540
6.6	183	555
7.0	186	567
7.1	194	606
7.2	205	627
nr	212	633
7.3	216	642
7.4	228	666
7.5	238	705
nr	257	753

‡ nr = not reported; * based on the SPECMAP oxygen isotope age model [57,58].

2.2. Seasonal Production of the Dust

It is assumed that the seasonal timing of Pleistocene dust input is similar to the modern dust input at the VM30–40 marine core site. We followed Prospero et al. [72], who studied the near-equatorial transport of West African dust across the Atlantic Ocean during calendar years 2002–2017. These authors showed significant increases in dust during winter and spring months using map-model observations generated from the Modern-Era Retrospective analysis for Research and Applications, Version 2 (MERRA—2). To illustrate the modern seasonality of dust plumes over the VM30–40 marine core site, we accessed 2002–2017 wet deposition products from the MERRA-2 generator. This tool is open-access through the NASA Giovanni website (Figure 2).

VM30–40 was retrieved at about 1400 km SW from the coast of West Africa and the site lies under the southern part of the winter and spring West African dust plumes (Figure 2). West African dust plumes are caused by the interrelated factors of the monsoon, the Intertropical Convergence Zone (ITCZ), and Hadley Cell convection. At the ITCZ, tradewinds meet as the easterly surface branch of Hadley Cells. Harmattan winds are part of the system of northeasterly tradewinds over North Africa. Harmattan winds are a main carrier of the winter and spring West African dust plume that flows southwest off the continent [12]. During the onset of the monsoon, sensible heating progressively moves northward across the African landmass to reach a maximum in boreal summer (JJA). The ocean–land temperature gradient that arises accelerates monsoonal winds landward to establish a deep tropical convection over northern Africa [73]. Tradewinds and the ITCZ follow sensible heating to the north. When the ITCZ migrates south during austral summer, the Harmattan winds extend over North African source areas to carry the winter dust plume [74]. Winter (DJF) dust plumes following a southwestern trajectory pass over the eastern equatorial Atlantic marine core site VM30–40 (Figure 2). In spring (MAM), West African dust activity continues (Figure 2) as the ITCZ migrates from south to north.

2.3. Analyses

Before the scanning of core VM30–40, the surfaces of its sections were scraped clean as standard protocol. The core sections were scanned lengthwise along the center of the core surface using an Itrax Core Scanner (Cox Analytical Systems, Mölndal, Sweden) at the Lamont-Doherty Earth Observatory Core Repository. Analyses were performed using settings of 30 kV and 30 mA with a Mo tube, a step size of 5 mm, and an exposure time of 5 s. The XRF data were collected in total counts [75], and we transformed the elemental data by calculating the log-ratios of the element intensities. Log-ratios have been shown to be simple linear functions of log-ratios of concentrations that minimize biases introduced by the analytical conditions of XRF measurements [76,77]. We selected the elements Si, Al, Rb, and Sr as proxy indicators of terrigenous material and paleoclimate. Si is used to represent the lithogenic quartz fraction in the dust and Al is probably a measure of the aluminum silicates of the finer clay minerals [23]. The grain size differences in these minerals are indicative of changing transport conditions such as wind strength [30]. Rb/Sr ratios of West African marine sediment cores indicate continental weathering intensity [61]. Sr-bearing carbonate phases are easily removed from soils and rock through dissolution, whereas the Rb is retained in K-bearing minerals like feldspar that are more resistant to weathering [78,79].

The log(Si/Al) and log(Rb/Sr) changes according to stratigraphic depth were constrained with the established $\delta^{18}O$ record of the core between 0 and 755 cm (Figure 3). Depth positions of MIS datums were used to construct a linear regression age model and scale the XRF depth series to time. The VM30–40 $\delta^{18}O$ record is from the planktonic foraminifera *Globigerinoides sacculifer* [57], and the data reported in Table B1 of McIntyre et al. [58] provide 28 core depths matched to 28 dates based on the SPECMAP oxygen isotope stratigraphy and marine isotope stages (Table 1). The timeseries for each of the log(ratio) were calibrated using the mean sedimentation rate of 1 cm per 340 years (Figure 3)

To assess orbital forcing, the log(Si/Al) and log(Rb/Sr) timeseries were resampled to the median sampling interval of 0.17 kyr, which corresponds to the step size of 5 mm used for the XRF scan of the core. We then treated each log(ratio) timeseries to spectral analysis using the Blackman–Tukey cross-coherency comparison method (B–T coherency for short). This was performed with the *AnalySeries* software (https://paloz.marum.de/confluence/display/ESPUBLIC/QAnalySeries-Public, accessed on 16 July 2024) [80]. Spectral analyses used a Bartlett window, and zero-coherency was set to an 0.5 (80%) level of significance. B–T coherency comparisons were made with eccentricity-tilt-precession (ETP) generated with *Acycle* software v2.8 [81,82].Gaussian and Tanner filters were applied to the XRF timeseries to isolate the significant orbital cycles identified from the B–T coherency method. The range of the filter was set based on significant frequencies resolved from the B–T coherency results and recommended settings [83]. Timeseries isolated from the filtering were then compared to the XRF stratigraphy, astronomical solutions, and the $\delta^{18}O$ proxy record of global ice volume obtained from the LR04 benthic stack [50].

3. Results

Neither of the two XRF timeseries for the core demonstrated a long-term directional shift toward higher or lower ratios (Figure 3). In addition to this broad similarity, the log(Rb/Sr) and log(Si/Al) timeseries had few features in common. Although frequent fluctuations occurred in both records, none of these appeared to be strongly synchronized, and the absolute maximum and minimum values were not in alignment or antiphase. As evident from the spectral analysis data presented below, the two XRF timeseries appeared to record different responses of West African dust to monsoon climate change over the last ~260 kyr. At some chronostratigraphic levels, the two records were antiphased but in different directions (Figure 3, compare MIS 1, MIS 2, and glacial maximum in MIS 6).

B–T coherency comparisons for the log(Rb/Sr) timeseries indicated significant frequencies of 22.7 and 18.2 kyr interpreted as climatic precession (Figure 4). For precession, the average period is roughly 21.5 kyr with a large dispersion between 14 and 30 kyr [84].

Other estimates suggest climatic precession ranges from 19 to 24 kyr with an average period of 21.5 kyr [85]. B–T coherency comparisons also suggested the presence of short eccentricity (Figure 4). This period may be related to the climate cycles indicated by the 18 kyr and 23 kyr precession signals [86]. However, the timespan of the core was probably too short to confirm the significance of low-frequency periods. Based on these observations, during the last ~260 kyr, Rb and Sr input to the marine core site was primarily driven by precessional variations in West African dust. The most likely process connecting precession to the Rb and Sr variations is orbital insolation changes.

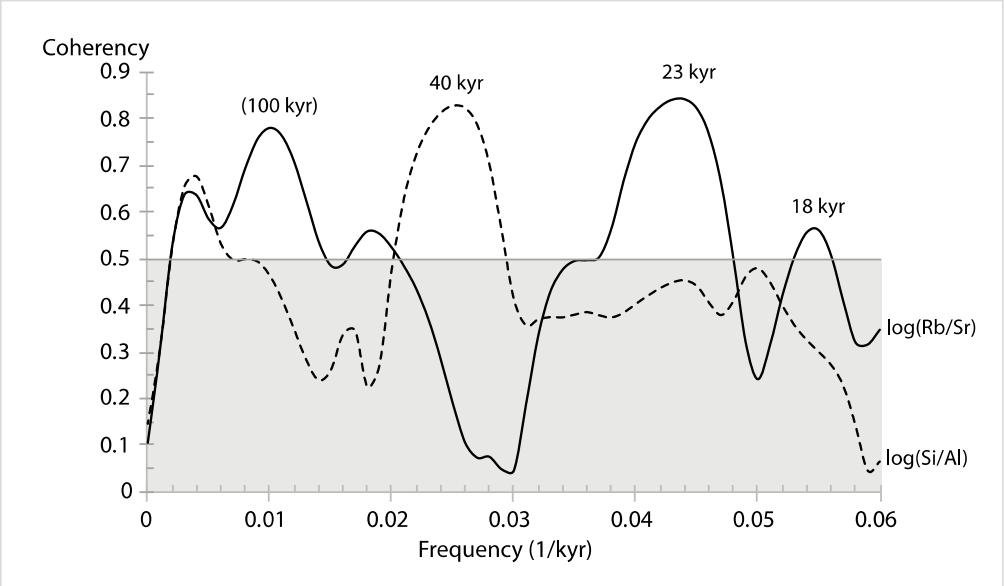

Figure 4. Results of Blackman–Tukey cross-coherency method. Frequency peaks below the gray-shaded area failed to achieve the 80% confidence interval. Periods correspond to short eccentricity (100 kyr), obliquity (40 kyr), and precession (23 and 18 kyr). A short eccentricity was probably not significant over the short timescale (~260 kyr) of this marine core.

Results for log(Si/Al) timeseries suggested a different spectrum of variability over the ~260 kyr record. Obliquity had high significance and was the dominant period indicated by the B–T coherency comparisons (Figure 4). No eccentricity or precession periods were demonstrated by the results. Several obliquity frequency components occurred with periods between ~40 and ~41 kyr, collectively resulting in the prominent ~40 kyr obliquity cycle [87]. The obliquity signals recognized from studies of late Pleistocene paleoclimate records had several different origins. For example, obliquity influenced fluctuations of glacial ice volume and atmospheric CO_2 concentrations despite late Pleistocene global climate change and sea level being dominated by eccentricity [88]. On the other hand, obliquity is regarded as an important control on intertropical insolation budgets that drive tropical paleoclimate change independent of glacial–interglacial conditions [39,89].

4. Discussion

4.1. Origin of the Precession Signal in the Rb/Sr Timeseries

Climatic precession affects the intensity of seasonality in the tropics [36]. It sets the distance from the Earth to the Sun at the summer solstice [84]. Since the monsoon is a seasonal insolation system, there is a strong relationship among precession, sensible heating of the African landmass, and tropical rainfall. Moisture and temperature changes during the late Quaternary of Africa were controlled by precession changes to insolation [29,38,90,91]. Moisture and temperature influence continental weathering rates, reflected in Rb and Sr concentrations [78,79,92,93].

Pokras and Mix [59] correlated the freshwater diatom increases in VM30–40 to dry monsoons during times of decreasing summer insolation (increasing precession). Lower lake levels in the summer were thought to increase the number of dry lakebeds that supplied detritus to subsequent winter dust plumes. However, freshwater diatom cycles are out of phase with precessional summer insolation (Figure 5A,B). Pokras and Mix [59] suggested that diatom sources were rapidly depleted during the early onset of dryness, accounting for the correlations between diatom maxima and the increasing limb of precession (decreasing limb of summer insolation) rather than at precession maxima (insolation minima). To assess the relationships between precessional insolation and the XRF elemental changes, we performed a phase analysis between the log(Rb/Sr) timeseries and the astronomical solution of insolation at 23° N for the mean monthly summer season (average over three months, JJA). Our results demonstrate that the two records are out of phase, with the XRF timeseries leading the precessional (23 kyr) summer insolation by about 90° or 6 kyr (Figure 6). This is not unlike the results of Pokras and Mix [59]. However, although not discussed in detail by these authors, it was also noted that the freshwater diatom increases in VM30–40 are approximately in phase with spring insolation (Figure 5C). An in-phase relationship with spring environmental processes is not unexpected given that modern West African dust plumes are active at this time of year [4,94,95]. Severe outbreaks of West African dust have been documented during March [96–98]. Spring dust deposition in the Caribbean and South America originates from fast-traveling, on the order of days, West African plumes that have equatorial trajectories across the Atlantic [72,99]. This is readily observed by model-map data that show springtime dust deposition over the core site VM30–40 in the eastern equatorial Atlantic (Figure 2). These low-latitude spring dust plumes probably relate to the position of the ITCZ and the tradewinds following SW trajectories off the northern African landmass [74]. To assess the presence of a spring insolation component to the XRF timeseries, an astronomical solution was generated for the spring season mean (MAM) at 23° N. The comparison suggests a strong in-phase relationship between the log(Rb/Sr) timeseries and spring insolation at the 23 kyr period of precession (Figure 6). Such a correlation between increased insolation and log(Rb/Sr) maxima agrees with observed modes of weathering. We associate increased North African moisture and temperature with higher insolation [89]. Greater Rb/Sr ratios are assumed to be indicative of stronger chemical weathering caused by increased moisture available for hydrolysis and higher temperatures that catalyze reactions [100]. Rb substitutes for the K ions found within more stable mineral phases [92]. K-rich micas and feldspars tend to be retained within soils and saprolites during chemical weathering [79,93]. It is expected that Rb/Sr typically increases with stronger chemical weathering because soluble Sr is removed or more Rb is retained [78,101]. Therefore, the higher Rb/Sr ratios correlating with the spring insolation maxima may be explained by stronger chemical weathering under hotter and wetter monsoonal climates. Moreover, Rb/Sr variations are well correlated with both increasing and decreasing spring insolation (Figure 7). This contrasts with the records of freshwater diatoms. The diatoms are physically weathered and only represent a portion of the insolation cycles, when lake levels drop below a threshold and detritus of dry lakebeds are incorporated into dust plumes. To explain the out-of-phase relationship between the diatom record and summer insolation, it has been suggested that the diatom maxima represent the brief input of *Melosira* to ocean sediments during the orbital climate transition between very humid conditions (annually high lake levels) and very arid conditions (annually low lake levels) [42,59,60].

However, absolute maximum values in the log(Rb/Sr) timeseries (Figure 3) coincide with the last glacial maximum of MIS 2 and the penultimate glacial maximum of MIS 6. These are generally regarded as dry times for North African climate [41,44]. This observation would appear to be in contrast with the above discussion that higher Rb/Sr ratios correlate with stronger chemical weathering under increased moisture and temperature. During the changeover from MIS 6 into 5 (Termination II), log(Rb/Sr) values decrease and reach a local minimum at ~125 Ka to coincide with the interglacial of MIS 5e (Figure 8).

In the interval through MIS 5 (~130–70 Ka), increased log(Rb/Sr) ratios occur near the end of stadial 5b and in the middle of stadial 5d (Figure 8). These patterns demonstrate higher ratios occur during dry glacial epochs, at odds with the higher ratios at increased temperature/moisture during insolation maxima (Figure 7A). A similar Rb/Sr climate incongruency was reported by Cole et al.'s [61] study of Pleistocene–Holocene West African dust from marine core sediments. During the last glacial maximum (MIS 2), increased Rb/Sr ratios were attributed to an increase in mechanical weathering over chemical weathering under a dry glacial climate [61,63]. "Softer" Sr-bearing minerals are thought to be readily affected by abrasion and subsequent dissolution. Evidence of glacial forcing from the B–T coherency data might lie with the significant ~100 kyr period in the log(Rb/Sr) (Figure 4). However, the core sequence (~260 kyr) is probably too short to make firm conclusions about 100 kyr cyclicity [32]. Furthermore, the ~100 kyr period in the log(Rb/Sr) B–T results (Figure 4) may represent the modulating effects of eccentricity on tropical insolation rather than a glacial signal [85,86]. Unambitiously, the spectral analyses (Figures 4, 6 and 7) demonstrate precessional insolation as a main control on the long-term variability in the Rb and Sr values. Variations in the log(Rb/Sr) timeseries during the aforementioned substages of MIS 5 are in phase with orbital precession (Figure 8). However, late Quaternary glacial cyclicity was sensitive to precession forcing of summer insolation [102]. The two records (Rb/Sr and glacial $\delta^{18}O$, e.g., Figure 8) may thus be indicative of separate responses to precession, rather than the Rb and Sr variations responding to the effects of global ice volume. There may be an underlying glacial imprint of mechanical weathering on the Rb and Sr data, but the magnitude of that remains to be determined.

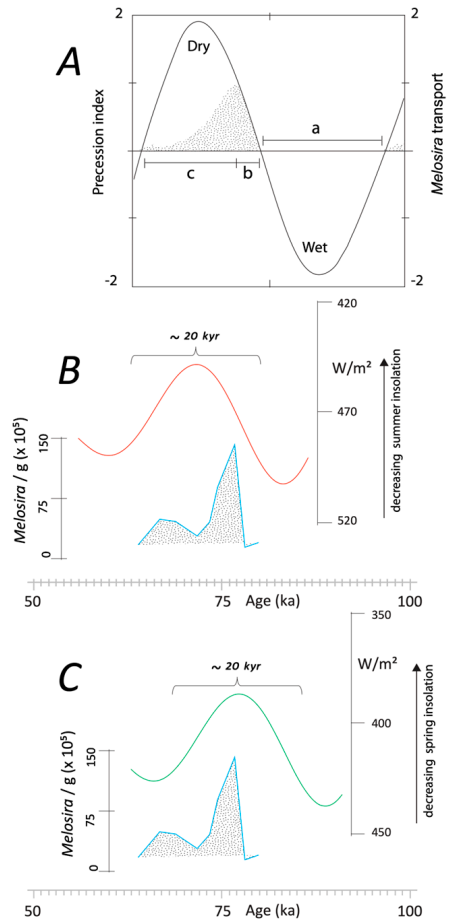

Figure 5. (**A**) Conceptual model of aeolian transport and deposition of freshwater diatoms in VM30–40 [59]. In the climatic precession curve, "a" is time of minimum precession (maximum insolation) and thus high lake levels, i.e., no diatom material available for transport. In "b", the onset of dryness

during increasing precession (decreasing insolation) quickly erodes and depletes sources of diatoms in the exposed lakebeds when lake level is low. In "c", very little diatom detritus is remaining for transport at the precession maximum (insolation minimum). (**B**) Pokras and Mix's [59] preferred chronostratigraphic correlation between diatom increases in the core (*Melosira*/g) and summer insolation. Example is shown for *Melosira* increase in the core near 75 ka. (**C**) Same as in (**B**) but spring insolation is now shown for comparison.

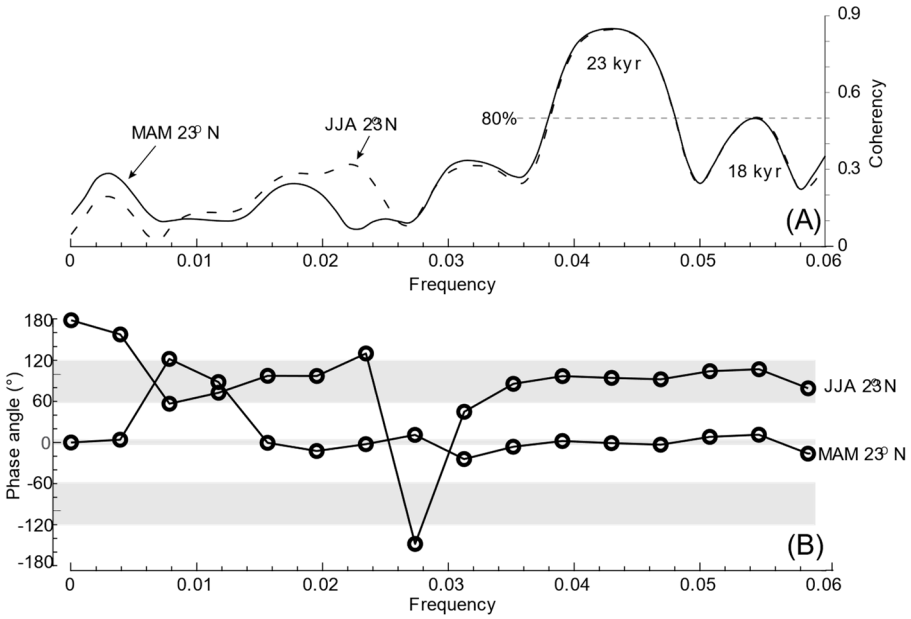

Figure 6. (**A**) Blackman–Tukey cross-coherency analysis [80] performed between the log(Rb/Sr) timeseries and seasonal insolation. (**B**) Phase relationship [81] between the log(Rb/Sr) timeseries and seasonal insolation for 23° north latitude.

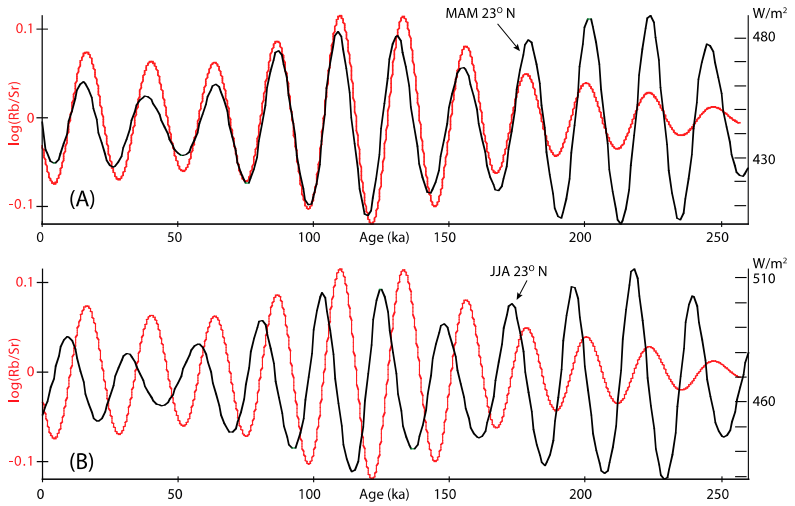

Figure 7. (**A**) The filtered precession log(Rb/Sr) timeseries compared to spring insolation. The Gaussian filter [80] was set at 0.036–0.048. (**B**) Same as previous, except with summer.

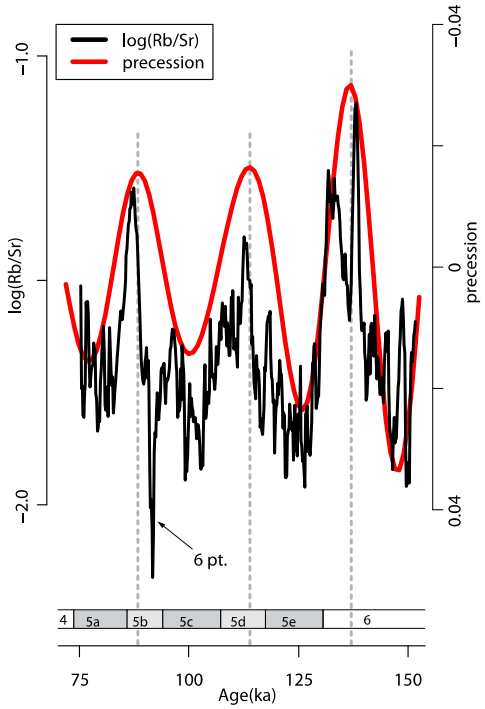

Figure 8. Chronostratigraphic comparison between the log(Rb/Sr) timeseries and orbital precession during late MIS 6 and into MIS 5. The log(Rb/Sr) data were smoothed with a 6-point moving average. Vertical dashed lines indicate position of precession minima.

4.2. Obliquity and Windiness in the Si/Al Data

Numerous types of marine core data have been used to study the Plio-Pleistocene terrigenous material and dust of North Africa, from rock magnetic parameters to pollen analyses [54,103]. Variation in the Si and Al contents of these cores represents changes in grain size, transport mode, and weatherability of continental detritus [48]. In the Mediterranean Basin, marine core sediments with increased Si/Al ratios are interpreted as proxy records of the intensified transport of (Si) eolian materials over the transport of (Al) fluvial materials from northern Africa [62]. Because West African river sediments are unlikely to reach the site of VM30–40, which is positioned near the crest of the Mid-Atlantic Ridge (2500 km west of Africa), the Al-rich fluvial materials may be wind-blown detritus from dry riverbeds/floodplains. Studies of Pleistocene West African marine core records have interpreted variations in Si/Al as proxy indications of Sahara–Sahel windiness [30,104].

Significant B–T results for the obliquity period (Figure 4) suggest the Si/Al ratios may be related to glacial–interglacial climate change. The glacial-related cooling of the sea surface temperature (SST) of the North Atlantic may weaken southwesterly winds carrying moist monsoonal air from the Gulf of Guinea [43]. A colder North Atlantic SST may lead to a slower/stoppage of the Atlantic Meridional Overturning Current (AMOC) and decreased transport of heat from southern to northern tropical waters [105]. Less warm water transport northward under slower AMOC causes a warmer South Atlantic Ocean [47]. This may lead to a more southern ITCZ position and dryer conditions over North Africa. Atlantic Ocean water heat transport affects the strength and location of the ITCZ and thus monsoonal rainfall over North Africa [49].

An ensemble of West African marine core sediment records [48] show that Al/Si ratios increase during a wet North African climate and decrease under dryness. Similar findings from other marine sediment core data suggest increased Si/Al ratios (dry) during glacial epochs and decreased Si/Al ratios (wet) during interglacials [30]. Over the last ~410 kyr of the Quaternary, high obliquity (interglacial) caused AMOC strength to increase and the ITCZ had a more northern position [106]. A more northern ITCZ suggests a wetter North

African monsoon [49]. A Tanner filter was used to isolate the significant obliquity period from the log(Si/Al) timeseries in Figure 4. Plotting these filtered data and comparing the timing with the Laskar et al. [82] solution reveals that the Si/Al variations are in phase with obliquity over the last ~260 kyr (Figure 9). This relationship is incongruent with the above expectations, as our data suggest Si/Al maxima during obliquity maxima (~wet interglacials) and minima during obliquity minima (~dry glacials). Therefore, the Si/Al variations in VM30–40 appear to reflect a paleoclimate control different from glacial forcing.

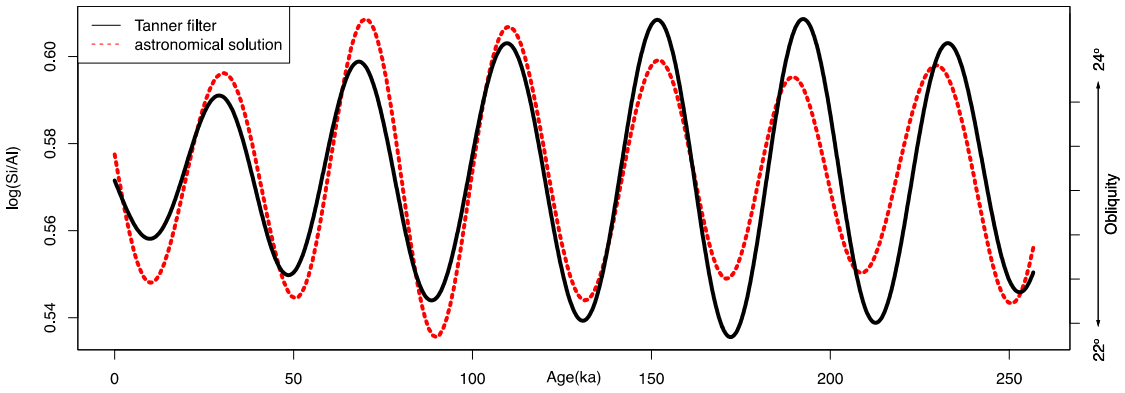

Figure 9. The filtered obliquity log(Si/Al) timeseries compared to the Laskar et al. [82] obliquity solution for the last ~260 kyr. The Tanner filter [83] was set at 0.022–0.029.

Instead of moisture variations, the Si/Al data may be indicative of Harmattan speed/strength. In modern times, the seasonal peak of Harmattan dust is thought to be more closely related to the ITCZ location and surface winds as compared to rainfall [28,74]. Climate model simulations indicate that the ITCZ position and the strength of the tradewinds is sensitive to cross-equatorial temperature gradients [107,108]. Obliquity insolation influences such gradients and causes differential warming of the northern and southern African tropics [39,89]. Increased obliquity is thought to be a cause of North Africa winters with stronger cross-equatorial winds [39]. Under increased obliquity, Hadley Cell convection over the winter hemisphere expands and intensifies, pushing the ITCZ and ascending branch of the Hadley Cell into the summer hemisphere [108]. This is accompanied by the enhancement of the tradewinds' intensities of the winter hemisphere and predominantly northerly surface wind anomalies near the equatorial latitudes [107]. These relationships may explain why the filtered log(Si/Al) timeseries is practically in phase with obliquity (Figure 9). A stronger/weaker Harmattan incorporates a greater/lesser amount of the larger silt-sized quartz particles into the dust plumes [30,104]. Obliquity affects the intensity of Harmattan winds by modulating the cross-equatorial insolation gradient [39].

4.3. $CaCO_3$ Dissolution Bias?

Some current studies on West African marine sediment core records of terrigenous material suggest that the glacial signals indicated by the dust fraction originate from the dissolution of carbonate phases in the core sediments [32]. The glacial–interglacial oscillations may be influencing the dust's sedimentary preservation context at the ocean bottom but not the dust production/transport from the Africa landmass [26]. During glacial epochs, deep ocean circulation changes bring corrosive southern-sourced deep waters to the eastern equatorial Atlantic [109]. The dissolution of the marine carbonate fraction leads to an overrepresentation of the terrigenous silicate fraction, which may cause a false positive for increased African dustiness. If carbonate dissolution has indeed impacted the VM30–40 core, then we expect to find evidence of decreased carbonate during glacial epochs and more carbonate during interglacials. Pokras [71] noted that for core VM30–40, carbonate percentages increase after glacial-to-interglacial shifts and decrease prior to interglacial-to-glacial transitions. A direct stratigraphic comparison (Figure 10) between

the LR04 $\delta^{18}O$ benthic stack (proxy of global ice volume) and the VM30–40 core percent carbonate (%$CaCO_3$) record reveals that many of the low %$CaCO_3$ values are associated with glacial epochs. A pronounced decrease to ~65% $CaCO_3$ occurs in MIS 2 (the last glacial maximum) and a decrease to <70% occurs in MIS 4. The transition from warm MIS 7 to glacial MIS 6 (penultimate glacial maximum) is marked by decreasing percentages that continue through to the late part of MIS 6. The MIS 7-to-MIS 6 transition is characterized by high maximum %$CaCO_3$ values in mid MIS 7, a pronounced drop to <65% in late MIS 7, intermediate maximum %$CaCO_3$ values in early MIS 6, a drop to <65% in mid MIS 6, and low maximum %$CaCO_3$ values in late MIS 6, followed by a pronounced drop to the lowest values of the core (<60%) in late MIS 6.

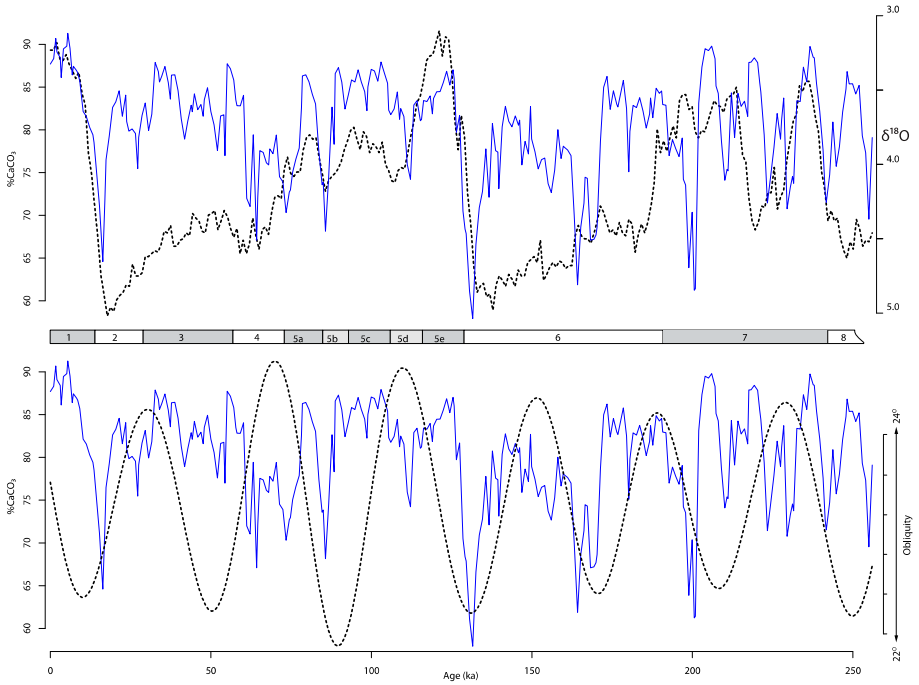

Figure 10. (**Upper**) The solid blue line is the %$CaCO_3$ record of the core (https://doi.org/10.1594/PANGAEA.51365) and the dotted line is the global ice volume record over the last ~260 kyr [50]. The scale along bottom depicts the MIS stages/substages. (**Lower**) Same as above except now the dotted line is the astronomical solution for obliquity [82].

In MIS 6, $CaCO_3$ variations follow the phase timing of orbital obliquity, in the manner predicted by the carbonate dissolution hypothesis. If carbonate is being dissolved during glacial epochs, then we should observe decreased %$CaCO_3$ at obliquity minima, when the icesheet volume expands. The VM30–40 record demonstrates increased %$CaCO_3$ near obliquity maxima and decreased %$CaCO_3$ during the obliquity minima of MIS 6.

Although we do not possess the data to completely understand the terrestrial and marine origins of carbonate in VM30–40, our Si/Al record should not be as affected by dissolution in comparison to $CaCO_3$. We are not measuring the total terrigenous fraction as calculated by terrigenous subtracted from carbonate; we are only measuring relative elemental ratios. Sr, however, replaces calcium in $CaCO_3$. Glacial dissolution on calcium-bearing Sr in VM30–40 may help to explain why the two largest Rb/Sr ratios of the core correlate with MIS 2 and MIS 6 glacial maxima. However, the B–T analysis of the log(Rb/Sr) timeseries indicates this was not a reoccurring disturbance, at least not on obliquity timescales. To further investigate the possible carbonate dissolution effects, we plotted individual Rb and Sr counts for the intervals of ~17–19.5 ka and ~133.5–137.5 ka (Figure 11). Each of these intervals constrain the two greatest weathering intensity maxima of the core. In both cases, the Sr decreases as the log(Rb/Sr) values become more negative, representing greater weathering. The decreased Sr could be an indication of the dissolution

of the carbonate-bearing phases that carry the Sr. However, the Rb counts are antiphase with the decreased Sr at ~17–19.5 ka yet have an in-phase decrease with decreased Sr at ~133.5–137.5 ka. This may suggest different Rb modes of weathering during glacial maxima.

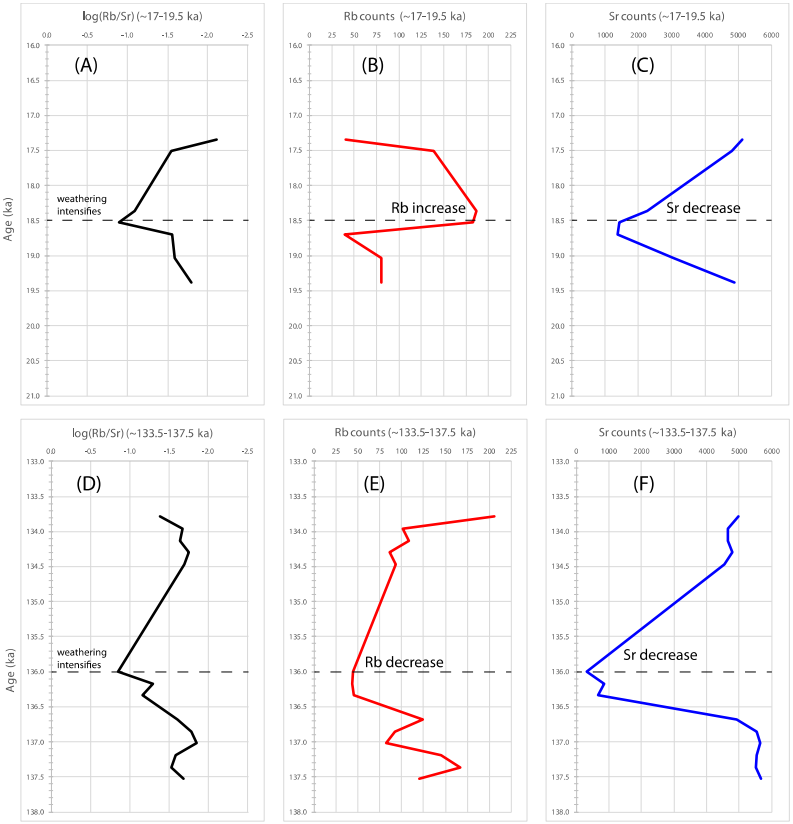

Figure 11. Comparison of weathering intensity (**A**), Rb counts (**B**), and Sr counts (**C**) during the last glacial maximum (MIS 2). Lower row of figures (**D**–**F**) is the same except for the penultimate glacial maximum (MIS 6).

5. Conclusions

XRF measurements were used to assess the late Quaternary (last ~260 kyr) elemental composition of marine sediment core VM30–40 from the eastern equatorial Atlantic Ocean, where the modern terrigenous input is dominated by winter and spring West African dust plumes associated with seasonal monsoonal dryness over the Sahel. A chronostratigraphic timeseries was constructed with previously determined marine oxygen isotope stages. Ratios of Rb to Sr (a proxy indicator of weathering) and Si to Al (grain size) revealed different orbital forcing patterns and correlations with proxy records of paleoclimate change. Although further work is necessary to independently validate our findings with other proxy records, the following conclusions are made from the collected data:

- Chemical weathering intensities (Rb/Sr) appear to be in phase with the timing of spring (MAM) insolation, presumably because of the moisture and temperature changes associated with the precession forcing of the West African monsoon.
- Grain size (Si/Al) maxima correlate to obliquity maxima, suggesting intensified winter tradewinds during interglacial epochs. This is inferred to reflect the sensitivity of the ITCZ over Africa to obliquity forcing of the intertropical insolation gradient [39].
- Maximum Rb/Sr values of the core coincide with the last glacial maximum (MIS 2) and the penultimate glacial maximum (MIS 6). Most paleoclimate reconstructions suggest that late Quaternary glacial epochs in northern Africa were cool and dry, which is at odds with chemical weathering intensities increasing (increasing Rb/Sr ratios) during warm and wet monsoons at spring insolation maxima. This may be

explained either by an increase in mechanical over chemical weathering during glacial epochs [61,63] or the dissolution of Sr-bearing phases of carbonate by corrosive glacial Atlantic bottom waters [32].

Supplementary Materials: The following supporting information can be downloaded at https://www.mdpi.com/article/10.3390/atmos15080902/s1: Table S1: Rb, Sr, Si, and Al XRF measurement values.

Author Contributions: C.J.L. conceived the idea for the research project. C.Y.C. helped to refine the research design. O.M.Y. and C.Y.C. performed XRF measurements. C.J.L., C.Y.C. and O.M.Y. analyzed the data. C.J.L. wrote the manuscript with contributions from C.Y.C. and O.M.Y. All authors have read and agreed to the published version of the manuscript.

Funding: Funding for this work was contributed by NSF REU award # 1757602 (D. Abbott and M. Kaplan) to Columbia University.

Data Availability Statement: Data are available free for public download. All data and reprints can be downloaded for free from the OSF data repository. Search for data_publications_Lepre. https://osf.io/b25h3/ (accessed on 16 July 2024).

Acknowledgments: We thank Maureen Raymo and Nichole Anest for access to the Lamont-Doherty Core Repository. Paul Olsen, Michael Kaplan, and Dallas Abbott helped organize the research cohort from which this work grew.

Conflicts of Interest: The authors declare no conflicts of interest.

References

1. Ojha, L.; Lewis, K.; Karunatillake, S.; Schmidt, M. The Medusae Fossae Formation as the single largest source of dust on Mars. *Nat. Commun.* **2018**, *9*, 2867. [CrossRef]
2. Soreghan, G.S.; Beccaletto, L.; Benison, K.C.; Bourquin, S.; Feulner, G.; Hamamura, N.; Hamilton, M.; Heavens, N.G.; Hinnov, L.; Huttenlocker, A.; et al. Report on ICDP Deep Dust workshops: Probing continental climate of the late Paleozoic icehouse–greenhouse transition and beyond. *Sci. Dril.* **2020**, *28*, 93–112. [CrossRef]
3. Jickells, T.D. Global Iron Connections Between Desert Dust, Ocean Biogeochemistry, and Climate. *Science* **2005**, *308*, 67–71. [CrossRef]
4. Barkley, A.E.; Prospero, J.M.; Mahowald, N.; Hamilton, D.S.; Popendorf, K.J.; Oehlert, A.M.; Pourmand, A.; Gatineau, A.; Panechou-Pulcherie, K.; Blackwelder, P.; et al. African biomass burning is a substantial source of phosphorus deposition to the Amazon, Tropical Atlantic Ocean, and Southern Ocean. *Proc. Natl. Acad. Sci. USA* **2019**, *116*, 16216–16221. [CrossRef]
5. Maher, B.A.; Prospero, J.M.; Mackie, D.; Gaiero, D.; Hesse, P.P.; Balkanski, Y. Global connections between aeolian dust, climate and ocean biogeochemistry at the present day and at the last glacial maximum. *Earth Sci. Rev.* **2010**, *99*, 61–97. [CrossRef]
6. Yuan, T.; Yu, H.; Chin, M.; Remer, L.A.; McGee, D.; Evan, A. Anthropogenic Decline of African Dust: Insights From the Holocene Records and Beyond. *Geophys. Res. Lett.* **2020**, *47*, e2020GL08971. [CrossRef] [PubMed]
7. Pitkanen-Brunnsberg, J. Background Note on the UN Sand and Dust Storm (SDS) Coalition. 2019. Available online: https://policycommons.net/artifacts/2227328/background-note-on-the-un-sand-and-dust-storm-sds-coalition/2984760/ (accessed on 16 July 2024).
8. Moskowitz, B.M.; Reynolds, R.L.; Goldstein, H.L.; Berquó, T.S.; Kokaly, R.F.; Bristow, C.S. Iron oxide minerals in dust-source sediments from the Bodélé Depression, Chad: Implications for radiative properties and Fe bioavailability of dust plumes from the Sahara. *Aeolian Res.* **2016**, *22*, 93–106. [CrossRef]
9. Washington, R.; Todd, M.C.; Engelstaedter, S.; Mbainayel, S.; Mitchell, F. Dust and the low-level circulation over the Bodélé Depression, Chad: Observations from BoDEx 2005. *J. Geophys. Res.* **2006**, *111*, D03201. [CrossRef]
10. Goudie, A.S.; Middleton, N.J. Saharan dust storms: Nature and consequences. *Earth-Sci. Rev.* **2001**, *56*, 179–204. [CrossRef]
11. Muhs, D.R. The geologic records of dust in the Quaternary. *Aeolian Res.* **2013**, *9*, 3–48. [CrossRef]
12. Schwanghart, W.; Schütt, B. Meteorological causes of Harmattan dust in West Africa. *Geomorphology* **2008**, *95*, 412–428. [CrossRef]
13. Akinsanola, A.A.; Zhou, W. Understanding the Variability of West African Summer Monsoon Rainfall: Contrasting Tropospheric Features and Monsoon Index. *Atmosphere* **2020**, *11*, 309. [CrossRef]
14. Peters, M.; Tetzlaff, G. The structure of West African Squall Lines and their environmental moisture budget. *Meteorl. Atmos. Phys.* **1988**, *39*, 74–84. [CrossRef]
15. Bercos-Hickey, E.; Nathan, T.R.; Chen, S.-H. On the Relationship between the African Easterly Jet, Saharan Mineral Dust Aerosols, and West African Precipitation. *J. Clim.* **2020**, *33*, 3533–3546. [CrossRef]
16. Nicholson, S.E. Climate of the Sahel and West Africa. In *Oxford Research Encyclopedia of Climate Science*; Oxford University Press: Oxford, UK, 2018. [CrossRef]

17. Rodríguez, S.; Calzolai, G.; Chiari, M.; Nava, S.; García, M.I.; López-Solano, J.; Marrero, C.; López-Darias, J.; Cuevas, E.; Alonso-Pérez, S.; et al. Rapid changes of dust geochemistry in the Saharan Air Layer linked to sources and meteorology. *Atmos. Environ.* **2020**, *223*, 117186. [CrossRef]
18. Blanco, A.; Dee Tomasi, F.; Filippo, E.; Manno, D.; Perrone, M.R.; Serra, A.; Tafuro, A.M.; Tepore, A. Characterization of African dust over southern Italy. *Atmos. Chem. Phys.* **2003**, *3*, 2147–2159. [CrossRef]
19. Rodriguez-Navarro, C.; di Lorenzo, F.; Elert, K. Mineralogy and physicochemical features of Saharan dust wet deposited in the Iberian Peninsula during an extreme red rain event. *Atmos. Chem. Phys.* **2018**, *18*, 10089–10122. [CrossRef]
20. McGee, D.; deMenocal, P.B.; Winckler, G.; Stuut, J.B.W.; Bradtmiller, L.I. The magnitude, timing and abruptness of changes in North African dust deposition over the last 20,000 yr. *Earth Planet. Sci. Lett.* **2013**, *371–372*, 163–176. [CrossRef]
21. Bonar, A.L.; Soreghan, G.S.; Elwood Madden, M.E. Assessing Weathering, Pedogenesis, and Silt Generation in Granitoid-Hosted Soils From Contrasting Hydroclimates. *JGR Earth Surf.* **2023**, *128*, e2023JF007095. [CrossRef]
22. Oldfield, F.; Chiverrell, R.C.; Lyons, R.; Williams, E.; Shen, Z.; Bristow, C.; Bloemendal, J.; Torrent, J.; Boyle, J.F. Discriminating dusts and dusts sources using magnetic properties and hematite:Goethite ratios of surface materials and dust from North Africa, the Atlantic and Barbados. *Aeolian Res.* **2014**, *13*, 91–104. [CrossRef]
23. Scheuvens, D.; Schütz, L.; Kandler, K.; Ebert, M.; Weinbruch, S. Bulk composition of northern African dust and its source sediments—A compilation. *Earth Sci. Rev.* **2013**, *116*, 170–194. [CrossRef]
24. Muhs, D.R.; Prospero, J.M.; Baddock, M.C.; Gill, T.E. Identifying Sources of Aeolian Mineral Dust: Present and Past. In *Mineral Dust*; Knippertz, P., Stuut, J.-B.W., Eds.; Springer: Dordrecht, The Netherlands, 2014; pp. 51–74. [CrossRef]
25. Armstrong, E.; Tallavaara, M.; Hopcroft, P.O.; Valdes, P.J. North African humid periods over the past 800,000 years. *Nat. Commun.* **2023**, *14*, 5549. [CrossRef] [PubMed]
26. Bozzano, G.; Kuhlmann, H.; Alonso, B. Storminess control over African dust input to the Moroccan Atlantic margin (NW Africa) at the time of maxima boreal summer insolation: A record of the last 220 kyr. *Palaeogeogr. Palaeoclimatol. Palaeoecol.* **2002**, *183*, 155–168. [CrossRef]
27. Crocker, A.J.; Naafs, B.D.A.; Westerhold, T.; James, R.H.; Cooper, M.J.; Röhl, U.; Pancost, R.D.; Xuan, C.; Osborne, C.P.; Beerling, D.J.; et al. Astronomically controlled aridity in the Sahara since at least 11 million years ago. *Nat. Geosci.* **2022**, *15*, 671–676. [CrossRef]
28. Kinsley, C.W.; Bradtmiller, L.I.; McGee, D.; Galgay, M.; Stuut, J.B.; Tjallingii, R.; Winckler, G.; DeMenocal, P.B. Orbital- and Millennial-Scale Variability in Northwest African Dust Emissions over the Past 67,000 years. *Paleoceanogr. Paleoclimatol.* **2022**, *37*, e2020PA004137. [CrossRef]
29. Kutzbach, J.E.; Guan, J.; He, F.; Cohen, A.S.; Orland, I.J.; Chen, G. African climate response to orbital and glacial forcing in 140,000-y simulation with implications for early modern human environments. *Proc. Natl. Acad. Sci. USA* **2020**, *117*, 2255–2264. [CrossRef]
30. Moreno, A.; Targarona, J.; Henderiks, J.; Canals, M.; Freudenthal, T.; Meggers, H. Orbital forcing of dust supply to the North Canary Basin over the last 250 kyr. *Quat. Sci. Rev.* **2001**, *20*, 1327–1339. [CrossRef]
31. O'Mara, N.A.; Skonieczny, C.; McGee, D.; Winckler, G.; Bory, A.J.M.; Bradtmiller, L.I.; Malaizé, B.; Polissar, P.J. Pleistocene drivers of Northwest African hydroclimate and vegetation. *Nat. Commun.* **2022**, *13*, 3552. [CrossRef]
32. Skonieczny, C.; McGee, D.; Winckler, G.; Bory, A.; Bradtmiller, L.I.; Kinsley, C.W.; Polissar, P.J.; De Pol-Holz, R.; Rossignol, L.; Malaizé, B. Monsoon-driven Saharan dust variability over the past 240,000 years. *Sci. Adv.* **2019**, *5*, eaav1887.
33. Tisserand, A.; Malaizé, B.; Jullien, E.; Zaragosi, S.; Charlier, K.; Grousset, F. African monsoon enhancement during the penultimate glacial period (MIS 6.5~170 ka) and its atmospheric impact. *Paleoceanography* **2009**, *24*, PA2220.
34. Trauth, M.H.; Larrasoaña, J.C.; Mudelsee, M. Trends, rhythms and events in Plio-Pleistocene African climate. *Quat. Sci. Rev.* **2009**, *28*, 399–411. [CrossRef]
35. Berger, A.; Loutre, M.F. Intertropical Latitudes and Precessional and Half-Precessional Cycles. *Science* **1997**, *278*, 1476–1478. [CrossRef]
36. Clement, A.C.; Hall, A.; Broccoli, A.J. The importance of precessional signals in the tropical climate. *Clim. Dyn.* **2004**, *22*, 327–341. [CrossRef]
37. Grant, K.M.; Amarathunga, U.; Amies, J.D.; Hu, P.; Qian, Y.; Penny, T.; Rodriguez-Sanz, L.; Zhao, X.; Heslop, D.; Liebrand, D.; et al. Organic carbon burial in Mediterranean sapropels intensified during Green Sahara Periods since 3.2 Myr ago. *Commun. Earth Environ.* **2022**, *3*, 11. [CrossRef]
38. Rossignol-Strick, M.; Nesteroff, W.; Olive, P.; Vergnaud-Grazzini, C. After the deluge: Mediterranean stagnation and sapropel formation. *Nature* **1982**, *295*, 105–110. [CrossRef]
39. Bosmans, J.H.C.; Hilgen, F.J.; Tuenter, E.; Lourens, L.J. Obliquity forcing of low-latitude climate. *Clim. Past.* **2015**, *11*, 1335–1346. [CrossRef]
40. Hennekam, R.; Grant, K.M.; Rohling, E.J.; Tjallingii, R.; Heslop, D.; Roberts, A.P.; Lourens, L.J.; Reichart, G.J. Accurately calibrated X-ray fluorescence core scanning (XRF-CS) record of Ti/Al reveals Early Pleistocene aridity and humidity variability over North Africa and its close relationship to low-latitude insolation. *Clim. Past* **2022**, *18*, 2509–2521. [CrossRef]
41. Castañeda, I.S.; Mulitza, S.; Schefuß, E.; Lopes dos Santos, R.A.; Sinninghe Damsté, J.S.; Schouten, S. Wet phases in the Sahara/Sahel region and human migration patterns in North Africa. *Proc. Natl. Acad. Sci. USA* **2009**, *106*, 20159–20163. [CrossRef] [PubMed]

42. deMenocal, P.B.; Ruddiman, W.F.; Pokras, E.M. Influences of High- and Low-Latitude Processes on African Terrestrial Climate: Pleistocene Eolian Records from Equatorial Atlantic Ocean Drilling Program Site 663. *Paleoceanography* **1993**, *8*, 209–242. [CrossRef]
43. deMenocal, P.D. Plio-Pleistocene African climate. *Science* **1995**, *270*, 53–59.
44. Gasse, F. Hydrological changes in the African tropics since the Last Glacial Maximum. *Quat. Sci. Rev.* **2000**, *19*, 189–211. [CrossRef]
45. Garcin, Y.; Vincens, A.; Williamson, D.; Buchet, G.; Guiot, J. Abrupt resumption of the African Monsoon at the Younger Dryas—Holocene climatic transition. *Quat. Sci. Rev.* **2007**, *26*, 690–704. [CrossRef]
46. Nicholson, S.E. Pleistocene and Holocene climates in Africa. *Nature* **1982**, *296*, 779. [CrossRef]
47. Chadwick, M.; Allen, C.S.; Sime, L.C.; Hillenbrand, C.-D. Analysing the timing of peak warming and minimum winter sea-ice extent in the Southern Ocean during MIS 5e. *Quat. Sci. Rev.* **2020**, *229*, 106134. [CrossRef]
48. Govin, A.; Varma, V.; Prange, M. Astronomically forced variations in western African rainfall (21°N-20°S) during the Last Interglacial period. *Geophys. Res. Lett.* **2014**, *41*, 2117–2125. [CrossRef]
49. Menviel, L.; Govin, A.; Avenas, A.; Meissner, K.J.; Grant, K.M.; Tzedakis, P.C. Drivers of the evolution and amplitude of African Humid Periods. *Commun. Earth Environ.* **2021**, *2*, 237. [CrossRef]
50. Lisiecki, L.E.; Raymo, M.E. A Pliocene-Pleistocene stack of 57 globally distributed benthic δ ^{18} O records. *Paleoceanography* **2005**, *20*, 2004PA001071. [CrossRef]
51. Bajo, P.; Drysdale, R.N.; Woodhead, J.D.; Hellstrom, J.C.; Hodell, D.; Ferretti, P.; Voelker, A.H.; Zanchetta, G.; Rodrigues, T.; Wolff, E.; et al. Persistent influence of obliquity on ice age terminations since the Middle Pleistocene transition. *Science* **2020**, *367*, 1235–1239. [CrossRef] [PubMed]
52. Clark, P.U.; Archer, D.; Pollard, D.; Blum, J.D.; Rial, J.A.; Brovkin, V.; Mix, A.C.; Pisias, N.G.; Roy, M. The middle Pleistocene transition: Characteristics, mechanisms, and implications for long-term changes in atmospheric pCO_2. *Quat. Sci. Rev.* **2006**, *25*, 3150–3184. [CrossRef]
53. Raymo, M.E.; Lisiecki, L.E.; Nisancioglu, K. Plio-Pleistocene Ice Volume, Antarctic Climate, and the Global d18O Record. *Science* **2006**, *313*, 492–495. [CrossRef]
54. Bloemendal, J.; deMenocal, P. Evidence for a change in the periodicity of tropical climate cycles at 2.4 Myr from whole-core magnetic susceptibility measurements. *Nature* **1989**, *342*, 897–900. [CrossRef]
55. Lepre, C.J.; Quinn, R.L. Aridification and orbital forcing of eastern African climate during the Plio-Pleistocene. *Glob. Planet. Chang.* **2022**, *208*, 103684. [CrossRef]
56. Trauth, M.H.; Asrat, A.; Berner, N.; Bibi, F.; Foerster, V.; Grove, M.; Kaboth-Bahr, S.; Maslin, M.A.; Mudelsee, M.; Schäbitz, F. Northern Hemisphere Glaciation, African climate and human evolution. *Quat. Sci. Rev.* **2021**, *268*, 107095. [CrossRef]
57. Imbrie, J.; Hays, J.D.; Martinson, D.G.; McIntyre, A.; Mix, A.C.; Morley, J.J.; Pisias, N.G.; Prell, W.L.; Shackleton, N.J. The orbital theory of Pleistocene climate: Support from a revised chronology of the marine $\delta^{18}O$ record. In *Milankovitch and Climate, Part 1*; Berger, A.L., Imbrie, J., Hays, J., Saltzman, B., Eds.; D. Reidel Publishing Co.: Dordrecht, The Netherlands, 1984; pp. 269–305.
58. McIntyre, A.; Ruddiman, W.F.; Karlin, K.; Mix, A.C. Surface water response of the equatorial Atlantic Ocean to orbital forcing. *Paleoceanography* **1989**, *4*, 19–55. [CrossRef]
59. Pokras, E.M.; Mix, A.C. Earth's precession cycle and Quaternary climatic change in tropical Africa. *Nature* **1987**, *326*, 486–487. [CrossRef]
60. Pokras, E.M.; Mix, A.C. Eolian Evidence for Spatial Variability of Late Quaternary Climates in Tropical Africa. *Quat. Res.* **1985**, *24*, 137–149. [CrossRef]
61. Cole, J.M.; Goldstein, S.L.; deMenocal, P.B.; Hemming, S.R.; Grousset, F.E. Contrasting compositions of Saharan dust in the eastern Atlantic Ocean during the last deglaciation and African Humid Period. *Earth Planet. Sci. Lett.* **2009**, *278*, 257–266. [CrossRef]
62. de Boer, B.; Peters, M.; Lourens, L.J. The Transient Impact of the African Monsoon on Plio-Pleistocene Mediterranean Sediments. *Clim. Past* **2020**, *17*, 331–344. [CrossRef]
63. Jung, S.J.A.; Davies, G.R.; Ganssen, G.M.; Kroon, D. Stepwise Holocene aridification in NE Africa deduced from dust-borne radiogenic isotope records. *Earth Planet. Sci. Lett.* **2004**, *221*, 27–37. [CrossRef]
64. Bradtmiller, L.I.; Anderson, R.F.; Fleisher, M.Q.; Burckle, L.H. Opal burial in the equatorial Atlantic Ocean over the last 30 ka: Implications for glacial-interglacial changes in the ocean silicon cycle. *Paleoceanography* **2007**, *22*, PA4216. [CrossRef]
65. Rowland, G.H.; Robinson, L.F.; Hendry, K.R.; Ng, H.C.; McGee, D.; McManus, J.F. The Spatial Distribution of Aeolian Dust and Terrigenous Fluxes in the Tropical Atlantic Ocean Since the Last Glacial Maximum. *Paleoceanogr. Paleoclimatology* **2021**, *36*, e2020PA004148. [CrossRef]
66. Tiedemann, R.; Sarnthein, M.; Shackleton, N.J. Astronomic timescale for the Pliocene Atlantic $\delta^{18}O$ and dust flux records of Ocean Drilling Program Site 659. *Paleoceanography* **1994**, *9*, 619–638. [CrossRef]
67. Hooghiemstra, H.; Lézine, A.-M.; Leroy, S.A.G.; Dupont, L.; Marret, F. Late Quaternary palynology in marine sediments: A synthesis of the understanding of pollen distribution patterns in the NW African setting. *Quat. Int.* **2006**, *148*, 29–44. [CrossRef]
68. Leroy, S.; Dupont, L. Development of vegetation and continental aridity in northwestern Africa during the Late Pliocene: The pollen record of ODP site 658. *Palaeogeogr. Palaeoclimatol. Palaeoecol.* **1994**, *109*, 295–316. [CrossRef]
69. Lézine, A.-M.; Casanova, J. Correlated oceanic and continental records demonstrate past climate and hydrology of North Africa (0–140 ka). *Geology* **1991**, *19*, 307. [CrossRef]
70. Balsam, W.L.; Otto-Bliesner, B.L.; Deaton, B.C. Modern and Last Glacial Maximum eolian sedimentation patterns in the Atlantic Ocean interpreted from sediment iron oxide content. *Paleoceanography* **1995**, *10*, 493–507. [CrossRef]

71. Pokras, E.M. Diatom record of Late Quaternary climatic change in the eastern equatorial Atlantic and tropical Africa. *Paleoceanography* **1987**, *2*, 273–286. [CrossRef]
72. Prospero, J.M.; Barkley, A.E.; Gaston, C.J.; Gatineau, A.; Campos y Sansano, A.; Panechou, K. Characterizing and Quantifying African Dust Transport and Deposition to South America: Implications for the Phosphorus Budget in the Amazon Basin. *Glob. Biogeochem. Cycles* **2020**, *34*, e2020GB006536. [CrossRef]
73. Sultan, B.; Janicot, S. Abrupt shift of the ITCZ over West Africa and intra-seasonal variability. *Geophys. Res. Lett.* **2000**, *27*, 3353–3356. [CrossRef]
74. Doherty, O.M.; Riemer, N.; Hameed, S. Control of Saharan mineral dust transport to Barbados in winter by the Intertropical Convergence Zone over West Africa. *J. Geophys. Res.* **2012**, *117*, 2012JD017767. [CrossRef]
75. Croudace, I.; Rothwell, G. Micro-XRF sediment core scanners: Important new tools for the environmental and earth sciences. *SpectroscopyEurope* **2010**, *22*, 6.
76. Hodell, D.; Lourens, L.; Crowhurst, S.; Konijnendijk, T.; Tjallingii, R.; Jiménez-Espejo, F.; Skinner, L.; Tzedakis, P.C.; Members, T.S.S.P.; Abrantes, F.; et al. A reference time scale for Site U1385 (Shackleton Site) on the SW Iberian Margin. *Glob. Planet. Chang.* **2015**, *133*, 49–64. [CrossRef]
77. Weltje, G.J.; Tjallingii, R. Calibration of XRF core scanners for quantitative geochemical logging of sediment cores: Theory and application. *Earth Planet. Sci. Lett.* **2008**, *274*, 423–438. [CrossRef]
78. Chen, J.; An, Z.; Head, J. Variation of Rb/Sr Ratios in the Loess-Paleosol Sequences of Central China during the Last 130,000 Years and Their Implications for Monsoon Paleoclimatology. *Quat. Res.* **1999**, *51*, 215–219. [CrossRef]
79. White, A.F.; Bullen, T.D.; Schulz, M.S.; Blum, A.E.; Huntington, T.G.; Peters, N.E. Differential rates of feldspar weathering in granitic regoliths. *Geochim. Cosmochim. Acta* **2001**, *65*, 847–869. [CrossRef]
80. Paillard, D.; Labeyrie, L.; Yiou, P. Macintosh Program performs time-series analysis. *Eos Trans. Am. Geophys. Union* **1996**, *77*, 379. [CrossRef]
81. Li, M.; Hinnov, L.; Kump, L. Acycle: Time-series analysis software for paleoclimate research and education. *Comput. Geosci.* **2019**, *127*, 12–22. [CrossRef]
82. Laskar, J.; Robutel, P.; Joutel, F.; Gastineau, M.; Correia, A.C.; Levrard, B. A long-term numerical solution for the insolation quantities of the Earth. *Astron. Astrophys.* **2004**, *428*, 261–285. [CrossRef]
83. Zeeden, C.; Kaboth, S.; Hilgen, F.J.; Laskar, J. Taner filter settings and automatic correlation optimisation for cyclostratigraphic studies. *Comput. Geosci.* **2018**, *119*, 18–28. [CrossRef]
84. Berger, A. Astronomical Frequencies in Paleoclimates. In *Encyclopedia of Marine Geosciences*; Harff, J., Meschede, M., Petersen, S., Thiede, J., Eds.; Springer: Dordrecht, The Netherlands, 2015; pp. 1–13. [CrossRef]
85. Olsen, P.E.; Laskar, J.; Kent, D.V.; Kinney, S.T.; Reynolds, D.J.; Sha, J.; Whiteside, J.H. Mapping Solar System chaos with the Geological Orrery. *Proc. Natl. Acad. Sci. USA* **2019**, *116*, 10664–10673. [CrossRef]
86. Berger, A.; Loutre, M.F.; Mélice, J.L. Equatorial insolation: From precession harmonics to eccentricity frequencies. *Clim. Past* **2006**, *2*, 131–136. [CrossRef]
87. Zeeden, C.; Meyers, S.R.; Hilgen, F.J.; Lourens, L.J.; Laskar, J. Time scale evaluation and the quantification of obliquity forcing. *Quat. Sci. Rev.* **2019**, *209*, 100–113. [CrossRef]
88. Clark, P.U.; Shakun, J.D.; Rosenthal, Y.; Köhler, P.; Bartlein, P.J. Global and regional temperature change over the past 4.5 million years. *Science* **2024**, *383*, 884–890. [CrossRef]
89. Tuenter, E.; Weber, S.L.; Hilgen, F.J.; Lourens, L.J. The response of the African summer monsoon to remote and local forcing due to precession and obliquity. *Glob. Planet. Chang.* **2003**, *36*, 219–235. [CrossRef]
90. Demenocal, P.; Ortiz, J.; Guilderson, T.; Adkins, J.; Sarnthein, M.; Baker, L.; Yarusinsky, M. Abrupt onset and termination of the African Humid Period: Rapid climate responses to gradual insolation forcing. *Quat. Sci. Rev.* **2000**, *19*, 347–361. [CrossRef]
91. Shanahan, T.M.; McKay, N.P.; Hughen, K.A.; Overpeck, J.T.; Otto-Bliesner, B.; Heil, C.W.; King, J.; Scholz, C.A.; Peck, J. The time-transgressive termination of the African Humid Period. *Nat. Geosci.* **2015**, *8*, 140–144. [CrossRef]
92. Blum, J.D.; Erel, I.Y.; Brown, K. $^{87}Sr/^{86}Sr$ ratios of Sierra Nevada stream waters: Implications for relative mineral weathering rates. *Geochim. Cosmochim. Acta* **1994**, *57*, 5019–5025. [CrossRef]
93. Blum, J.D.; Erel, Y. Rb-Sr isotope systematics of a granitic soil chronosequence: The importance of biotite weathering. *Geochim. Cosmochim. Acta* **1997**, *61*, 3193–3204. [CrossRef]
94. Marticorena, B.; Chatenet, B.; Rajot, J.L.; Traoré, S.; Coulibaly, M.; Diallo, A.; Koné, I.; Maman, A.; NDiaye, T.; Zakou, A. Temporal variability of mineral dust concentrations over West Africa: Analyses of a pluriannual monitoring from the AMMA Sahelian Dust Transect. *Atmos. Chem. Phys.* **2010**, *10*, 8899–8915. [CrossRef]
95. Prospero, J.M.; Glaccum, R.A.; Nees, R.T. Atmospheric transport of soil dust from Africa to South America. *Nature* **1981**, *289*, 570–572. [CrossRef]
96. Gläser, G.; Knippertz, P.; Heinold, B. Orographic Effects and Evaporative Cooling along a Subtropical Cold Front: The Case of the Spectacular Saharan Dust Outbreak of March 2004. *Mon. Weather. Rev.* **2012**, *140*, 2520–2533. [CrossRef]
97. Knippertz, P.; Fink, A.H. Synoptic and dynamic aspects of an extreme springtime Saharan dust outbreak. *Quart. J. R. Meteoro Soc.* **2006**, *132*, 1153–1177. [CrossRef]
98. Tulet, P.; Mallet, M.; Pont, V.; Pelon, J.; Boone, A. The 7–13 March 2006 dust storm over West Africa: Generation, transport, and vertical stratification. *J. Geophys. Res.* **2008**, *113*, 2008JD009871. [CrossRef]

99. Prospero, J.M.; Collard, F.-X.; Molinié, J.; Jeannot, A. Characterizing the annual cycle of African dust transport to the Caribbean Basin and South America and its impact on the environment and air quality: African dust transport to South America. *Global Biogeochem. Cycles* **2014**, *28*, 757–773. [CrossRef]
100. Kump, L.R.; Brantley, S.L.; Arthur, M.A. Chemical Weathering, Atmospheric CO_2, and Climate. *Annu. Rev. Earth Planet. Sci.* **2000**, *28*, 611–667. [CrossRef]
101. Hemming, S.R. Terrigenous Sediments. In *Encyclopedia of Quaternary Science*; Elsevier: Oxford, UK, 2007; Volume 3, pp. 1776–1785.
102. Hobart, B.; Lisiecki, L.E.; Rand, D.; Lee, T.; Lawrence, C.E. Late Pleistocene 100-kyr glacial cycles paced by precession forcing of summer insolation. *Nat. Geosci.* **2023**, *16*, 717–722.
103. Dupont, L. Orbital scale vegetation change in Africa. *Quat. Sci. Rev.* **2011**, *30*, 3589–3602. [CrossRef]
104. Moreno, T.; Querol, X.; Castillo, S.; Alastuey, A.; Cuevas, E.; Herrmann, L.; Mounkaila, M.; Elvira, J.; Gibbons, W. Geochemical variations in aeolian mineral particles from the Sahara–Sahel Dust Corridor. *Chemosphere* **2006**, *65*, 261–270. [CrossRef]
105. McManus, J.F.; Francois, R.; Gherardi, J.-M.; Keigwin, L.D.; Brown-Leger, S. Collapse and rapid resumption of Atlantic meridional circulation linked to deglacial climate changes. *Nature* **2004**, *428*, 834–837. [CrossRef]
106. Zhang, P.; Xu, J.; Holbourn, A.; Kuhnt, W.; Xiong, Z.; Li, T. Obliquity Induced Latitudinal Migration of the Intertropical Convergence Zone During the Past ∼410 kyr. *Geophys. Res. Lett.* **2022**, *49*, e2022GL100039. [CrossRef]
107. Broccoli, A.J.; Dahl, K.A.; Stouffer, R.J. Response of the ITCZ to Northern Hemisphere cooling. *Geophys. Res. Lett.* **2006**, *33*, L01702. [CrossRef]
108. Mantsis, D.F.; Lintner, B.R.; Broccoli, A.J.; Erb, M.P.; Clement, A.C.; Park, H.S. The Response of Large-Scale Circulation to Obliquity-Induced Changes in Meridional Heating Gradients. *J. Clim.* **2014**, *27*, 5504–5516. [CrossRef]
109. Oppo, D.W.; Fairbanks, R.G. Variability in the deep and intermediate water circulation of the Atlantic Ocean during the past 25,000 years: Northern Hemisphere modulation of the Southern Ocean. *Earth Planet. Sci. Lett.* **1987**, *86*, 1–15. [CrossRef]

Disclaimer/Publisher's Note: The statements, opinions and data contained in all publications are solely those of the individual author(s) and contributor(s) and not of MDPI and/or the editor(s). MDPI and/or the editor(s) disclaim responsibility for any injury to people or property resulting from any ideas, methods, instructions or products referred to in the content.